



Equivalent permeability and permittivity of Sm substituted Mg–Cd ferrites for high-frequency applications



Gongwen Gan^{a,*}, Dainan Zhang^{a,**}, Jie Li^a, Gang Wang^a, Xin Huang^a, Yan Yang^a, Yiheng Rao^a, Fang Xu^a, Xueying Wang^a, Huaiwu Zhang^a, Ray T. Chen^b

^a State Key Laboratory of Electronic Thin Films and Integrated Devices, University of Electronic Science and Technology of China, Chengdu, 610054, China

^b Microelectronic Research Center, Department of Electrical and Computer Engineering, University of Texas at Austin, Austin, TX, 78758, USA

ARTICLE INFO

Article history:

Received 4 September 2019

Received in revised form

14 November 2019

Accepted 15 November 2019

Available online 16 November 2019

Keywords:

Mg_{0.8}Cd_{0.2}Fe_{2-x}Sm_xO₄ composites

Enhanced magnetization

Equivalent permeability and permittivity

Low loss

ABSTRACT

The effects of Sm³⁺ ion substitution on the magnetic and dielectric properties of Mg ferrites (Mg_{0.8}Cd_{0.2}Fe_{2-x}Sm_xO₄) with 2.5 wt% Bi₂O₃ were investigated for use as high-frequency antenna substrates. Various concentrations of Sm³⁺ ions (x = 0.00, 0.02, 0.04, 0.06, 0.08 and 0.10) were employed to modify the permeability (μ') and permittivity (ϵ') of the ferrites. Experimentally, the composites synthesized using the conventional solid-state reaction method exhibited equal μ' and ϵ' (x = 0.10, $\mu' \approx 23\text{H/m}$, $\epsilon' \approx 25\text{F/m}$) over a long frequency band covering 1 MHz–100 MHz. Low loss tangents (dielectric loss $\tan\delta_\epsilon \approx 0.004$ and magnetic loss $\tan\delta_\mu \approx 0.038$) were also obtained over the same frequency range. Furthermore, a saturation magnetization of up to 24.45 emu/g and coercivity of up to 36 Oe were achieved when x increased to 0.10, indicating that the magnetization of the samples was enhanced. The excellent properties obtained in the Sm³⁺ substituted Mg ferrites suggest that they could be promising candidates for modern high-frequency antenna substrates.

© 2019 Elsevier B.V. All rights reserved.

1. Introduction

Miniaturization is the greatest requirement of modern antennas operating at frequencies such as high frequency (HF) (3–30 MHz) and very high frequency (VHF) (30–300 MHz) bands. Generally, it is not possible to use conventional antennas with a large physical size [1]. One method to reduce the physical dimension of antennas is to apply a class of material with high refractive index n ($n = \sqrt{\mu'\epsilon'}$), which can be obtained by adapting the materials with a high value of permeability (μ') and permittivity (ϵ') according to the relationship [2]:

$$l \propto \frac{1}{f_r n}$$

Where l is the antenna patch length and f_r is the resonance frequency. This relationship indicates that if the resonance frequency is fixed, the higher n is, the lower l will be. However, exceedingly

high permittivity can excite surface waves and trap them in the antenna substrate, which results in more mutual coupling between antenna arrays [3,4]. Therefore, the radiation efficiency is lowered and radiation pattern is attenuated. Based on this, it is quite important to explore substrate materials with moderate permittivity suitable for the requirement. With equivalent μ' and ϵ' , these materials achieve excellent impedance matching between the antenna and free space when serving as an antenna substrate. This can be explained using the following equation [5,6]:

$$Z = \sqrt{\frac{\mu' \mu'_0}{\epsilon' \epsilon'_0}} = \eta_0 \sqrt{\frac{\mu'}{\epsilon'}}$$

Where Z is the impedance of the antenna, η_0 is the impedance of free space, and is equal to $\sqrt{\frac{\mu_0}{\epsilon_0}}$. If $\sqrt{\frac{\mu'}{\epsilon'}}$ is approximately equal to 1, Z will approximately become equal to η_0 . Consequently, when the antenna radiates, unnecessary energy loss due to reflections caused by a mismatched impedance between the antenna and free space can be eliminated [7]. From the perspective of efficiency, the loss of energy due to heat resulting from the loss tangents lowers the performance of the antenna, and hence the loss tangents (the

* Corresponding author.

** Corresponding author.

E-mail addresses: dnzhang@uestc.edu.cn (D. Zhang), chenrt@austin.utexas.edu (R.T. Chen).

magnetic loss tangent $\tan\delta_{\mu}$ and dielectric loss tangent $\tan\delta_{\epsilon}$ should be sufficiently small [8].

Recent investigations of the magnetic and dielectric properties of ferrites tuned by introducing rare-earth cations such as Sm^{3+} , La^{3+} , Nd^{3+} , and Gd^{3+} etc, which give rise to a higher anisotropy constant and enhanced magnetization, have been conducted by many researchers [9–11]. The rare earth ions with a 4f orbital are totally screened by 5s and 5p orbitals that have a dominating position in tuning the electrical and magnetic properties of ferrites [12]. Meanwhile, magnesium ferrite with a spinel structure is a kind of soft magnetic material that can be a promising candidate for high-frequency applications due to its excellent magnetic and dielectric performance, along with its physical and chemical stability [13]. In our previous work, a study of the magneto-dielectric properties of Cd-substituted Mg ferrites with a Bi_2O_3 dopant for high-frequency antennas was carried out to realize the equivalence of μ' and ϵ' [6,14].

The objective of this study is to investigate the magneto-dielectric properties by designing a kind of modified Mg–Cd ferrite by substituting Fe^{3+} with Sm^{3+} ions using the formula $\text{Mg}_{0.8}\text{Cd}_{0.2}\text{Fe}_{2-x}\text{Sm}_x\text{O}_4$ ($x = 0.00, 0.02, 0.04, 0.06, 0.08$ and 0.10). With various concentrations of Sm^{3+} ions, magnetization, magnetic, and dielectric spectra are characterized by correlating with the changes in the microstructure. Finally, equivalent permeability and permittivity samples with low loss tangent and excellent magnetic properties are obtained.

2. Experiment

The proposed samples with formula $\text{Mg}_{0.8}\text{Cd}_{0.2}\text{Fe}_{2-x}\text{Sm}_x\text{O}_4$ ($x = 0.00, 0.02, 0.04, 0.06, 0.08$ and 0.10) were synthesized using the conventional solid-state reaction method. Pure original materials, MgO (AR grade, $\geq 99\%$), CdO (AR grade, $\geq 99\%$), Co_2O_3 (AR grade, $\geq 99\%$), Sm_2O_3 (AR grade, $\geq 99\%$), Fe_2O_3 (AR grade, $\geq 99\%$), and Bi_2O_3 (AR grade, $\geq 99\%$) were mixed in a calculated proportion, and were ball-milled for the first time in a planetary mixer for 12 h. Next, they were dried and pre-sintered at 1100°C for 4 h to realize the initial reaction. The powder was then ball-milled a second time with 2.5 wt% Bi_2O_3 to realize low temperature sintering for another 12 h. All the dried powder was pelletized by adding polyvinyl alcohol (PVA). Next, the particles were pressed into wafers and rings in a mold under the pressure of 10 MPa. Finally, low temperature sintering of the molded samples was conducted at 950°C .

The crystallography and phase analysis of the samples was measured using X-ray diffraction (XRD) (DX-2700, Haoyuan Co.) with Cu–K α radiation at a geometric angle of θ - 2θ varying from 10° to 80° with the angle increasing rate of 0.03° per second. Then Rietveld refinement was employed to calibrate the measured XRD results using GSAS refinement software. The magnetic hysteresis loops of the composites were measured using a vibrating sample magnetometer (VSM) (MODEL, BHL-525) with magnetic field ranging from -2500 Oe to 2500 Oe. The magnetic and dielectric behaviors were investigated using an HP-42391B RF impedance analyzer with frequency varying from 1 MHz to 1.5 GHz. The microstructure analysis was performed using a scanning electron microscope (SEM) (JEOL, JSM-6490) with a magnification of 3400. An auto density tester (GF-300D, AND Co.) was applied to measure the bulk density using the Archimedes' principle. All the measurements were performed at room temperature.

3. Results and discussion

The XRD measurements were performed to investigate the crystallography and phase of the samples (see Fig. 1). It can be observed that there is no other impurity peak detected besides the

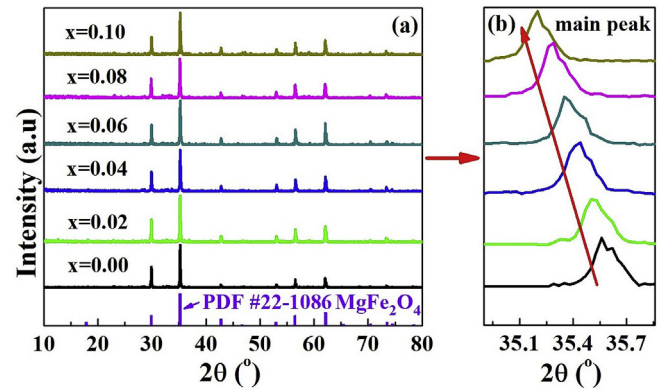


Fig. 1. X-ray powder diffraction patterns for $\text{Mg}_{0.8}\text{Cd}_{0.2}\text{Fe}_{2-x}\text{Sm}_x\text{O}_4$ samples with $x = 0.00$ – 0.10 , compared to the standard pattern of MgFe_2O_4 . (a) The full measurement range of 2θ , (b) an expanded view of the region around 35° of 2θ .

normal spinel peaks indexed to standard MgFe_2O_4 peaks, referred to as standard PDF card files, No. 22–1086. All the diffraction peaks are in good agreement with the indexed peaks, indicating that intrinsic crystalline structure of spinel Mg ferrites is unmodified despite Sm^{3+} ions substituting Fe^{3+} ions. These patterns indicate that the introduced Bi_2O_3 did not generate a second phase due to the Bi^{3+} ions in the small Bi_2O_3 fraction flowing into the lattice of the spinel phase. This is because if the temperature exceeds 900°C , Bi^{3+} ions begin to transform into the liquid state, and even evaporate when the synthesizing temperature of Bi–Fe oxide is not higher than 900°C [15]. Meanwhile, a slight shift of peaks towards left is observed as x increases from 0.00 to 0.10, as the enlarged figure of main peak shown in Fig. 1 (b). This is due to the increase in lattice constant because of the large ionic radius of Sm^{3+} ions compared to Fe^{3+} ions and the increasing Sm^{3+} ion concentration [16,17].

The results for Rietveld refinement are displayed in Fig. 2, which shows the observed, calculated and the difference between the observed and calculated patterns. And the specific results for the X-ray powder diffraction patterns with lattice constant, the cations occupying at A site and B site, goodness of reliability (χ^2 , ωR_p and R_p), and the occupation of Sm ions are shown in Table 1. It is noticed that the substituting Sm^{3+} ions occupy at octahedral (B) site despite changeable Sm concentration. As Sm concentration increases, a fraction of Mg ions migrate from A to B site, while some Fe ions migrate in the opposite direction. Meanwhile, lattice constant still increases with increasing Sm concentration, as mentioned before. Meanwhile, the effect of different sintering temperatures on the theoretical density (ρ_T) for all samples are calculated by Rietveld refinement using the equation [18]: $\rho_T = \frac{8M_w}{N_A \times a^3}$. And the numerical results are listed in Table 2.

The morphology of the ferrites synthesized with various Sm^{3+} ion concentrations is shown in Fig. 3. It can be observed that the ferrites definitely have spinel construction. There is an evident change in grain size and densification, which play key roles in determining magnetic and dielectric properties. The grain size first increases monotonously as x increases from 0.00 to 0.06. The grain size then drops off as x continuously increases up to 0.10.

The grain growth is mainly determined by the mobility of grain boundaries in the sintering process from two aspects. The first one is grain boundary diffusivity for host ions is changed by the defect chemistry and the dopant-defect associations [19], the increase in grain size in this study is attributed to the higher mobility of Sm^{3+} ions caused liquid phase sintering [17,20,21], which flows into gaps between grains and assists to grain growth. The second factor is the

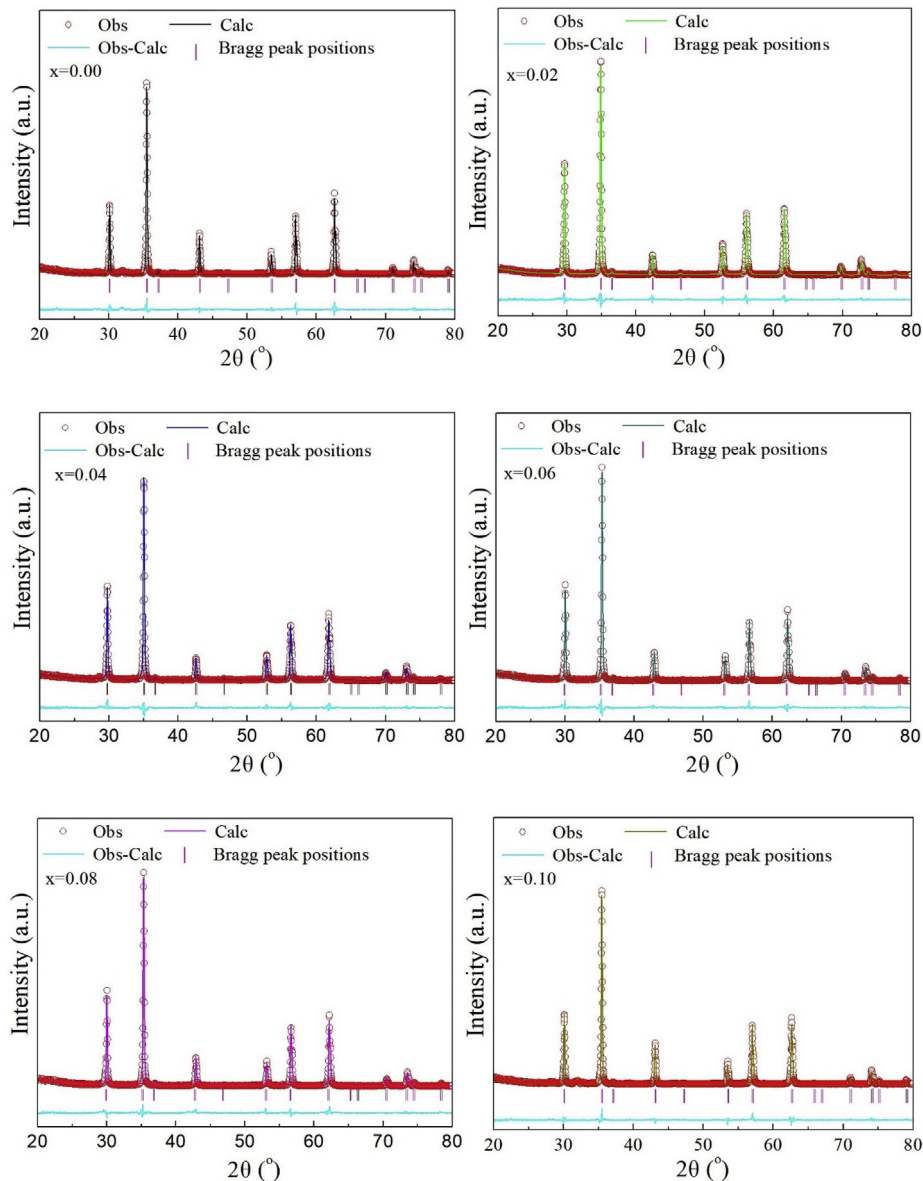


Fig. 2. Rietveld refinement results for the X-ray powder diffraction patterns of $\text{Mg}_{0.8}\text{Cd}_{0.2}\text{Fe}_{2-x}\text{Sm}_x\text{O}_4$ samples with different Sm^{3+} ions, the observed patterns (rings in red), the best fit Rietveld profiles (calculated, lines in various colors corresponding to XRD patterns), and difference between the observed pattern and the best-fit Rietveld profiles (cyan solid line) and Bragg peak positions (pink vertical line segments). (For interpretation of the references to color in this figure legend, the reader is referred to the Web version of this article.)

Table 1

Rietveld refinement results for the X-ray powder diffraction sample patterns with A-site ions, B-site ions, lattice constant (L_c) (with standard deviation), χ^2 , ωRp , Rp , and the occupation of Sm (S_o) ions for various Sm content (S_c).

S_c	A site	B site	L_c (Å)	χ^2	ωRp	Rp	S_o
0.00	$(\text{Mg}^{2+}_{0.48}\text{Cd}^{2+}_{0.2}\text{Fe}^{3+}_{0.32})$	$[\text{Mg}^{2+}_{0.32}\text{Fe}^{3+}_{1.68}]$	8.4531 (2)	1.81	9.76%	8.56%	–
0.02	$(\text{Mg}^{2+}_{0.47}\text{Cd}^{2+}_{0.2}\text{Fe}^{3+}_{0.33})$	$[\text{Mg}^{2+}_{0.33}\text{Sm}^{3+}_{0.02}\text{Fe}^{3+}_{1.65}]$	8.4696 (4)	1.85	10.01%	8.92%	B site
0.04	$(\text{Mg}^{2+}_{0.45}\text{Cd}^{2+}_{0.2}\text{Fe}^{3+}_{0.35})$	$[\text{Mg}^{2+}_{0.35}\text{Sm}^{3+}_{0.04}\text{Fe}^{3+}_{1.61}]$	8.4755 (1)	1.94	10.87%	10.04	B site
0.06	$(\text{Mg}^{2+}_{0.45}\text{Cd}^{2+}_{0.2}\text{Fe}^{3+}_{0.35})$	$[\text{Mg}^{2+}_{0.36}\text{Sm}^{3+}_{0.06}\text{Fe}^{3+}_{1.59}]$	8.4826 (2)	1.76	8.98%	7.89%	B site
0.08	$(\text{Mg}^{2+}_{0.44}\text{Cd}^{2+}_{0.2}\text{Fe}^{3+}_{0.33})$	$[\text{Mg}^{2+}_{0.36}\text{Sm}^{3+}_{0.08}\text{Fe}^{3+}_{1.59}]$	8.4903 (3)	2.19	11.73%	10.16%	B site
0.10	$(\text{Mg}^{2+}_{0.43}\text{Cd}^{2+}_{0.2}\text{Fe}^{3+}_{0.33})$	$[\text{Mg}^{2+}_{0.37}\text{Sm}^{3+}_{0.10}\text{Fe}^{3+}_{1.57}]$	8.5011 (5)	2.03	10.85%	10.28%	B site

amount of doped ions that segregates at the grain boundary and restrains the grain boundary movement. When the amount exceeds 0.06, the decrease in grain size is observed with the appearance of agglomerated grains and open areas because deposition of Sm^{3+} ions on the grain boundaries [19,21,22]. The average grain size

reflected in Table 2 is evaluated using the Scherrer equation that complies with the crystalline nature. Regarding the densification, the samples first become denser due to less pores between grains, when x increases from 0.00 to 0.06, and then become sparser due to more appearance of pores, which results in the decrease in bulk

Table 2
Average grain size (AGZ), theoretical density (ρ_T), experimental density (ρ_B), and relative density (ρ_R) of $Mg_{0.8}Cd_{0.2}Fe_{2-x}Sm_xO_4$ samples with $x = 0.00-0.10$.

x value	0.00	0.02	0.04	0.06	0.08	0.10
AGZ (μm)	2.97	3.12	3.43	3.89	2.78	2.64
ρ_T (g/cm^3)	4.871	5.034	5.060	5.096	5.047	4.99
ρ_B (g/cm^3)	4.445	4.647	4.711	4.771	4.645	4.511
ρ_R (%)	91.26	92.32	93.11	93.62	92.07	90.42

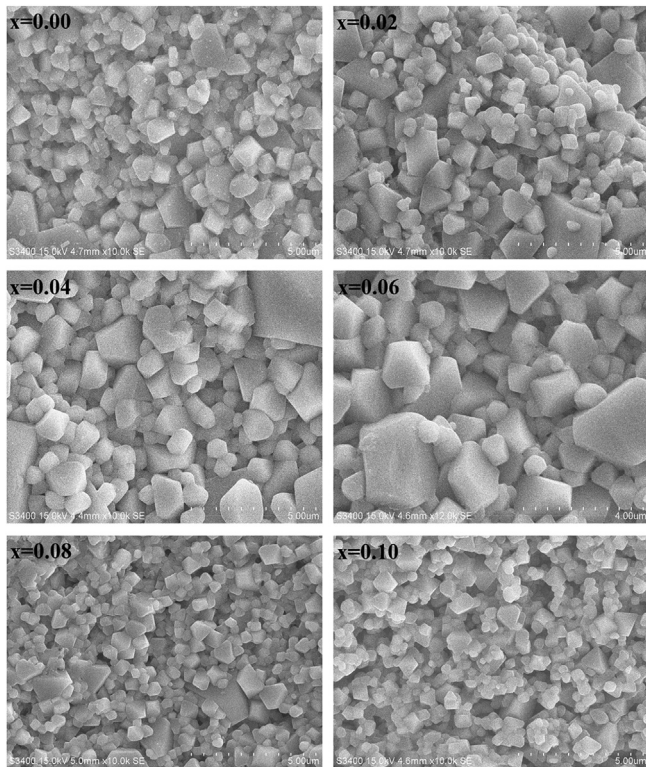


Fig. 3. Morphology of the synthesized $Mg_{0.8}Cd_{0.2}Fe_{2-x}Sm_xO_4$ samples with $x = 0.00-0.10$.

density, as x increases to 0.10. In other words, the samples exhibit the same tendency for change in porosity and grain size. Fig. 4 and Table 2 display the change in the experimental bulk density (ρ_B)

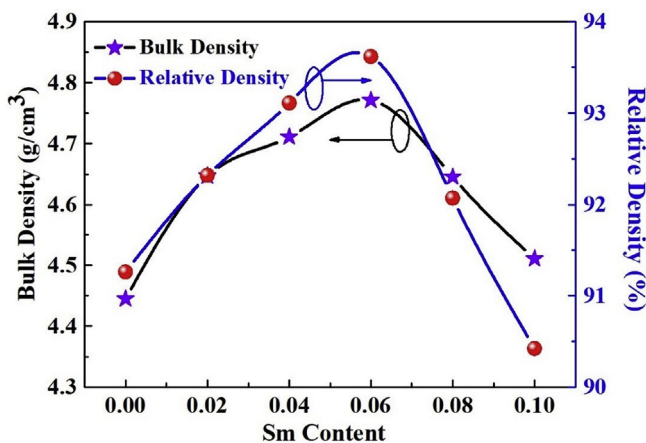


Fig. 4. Experimental bulk density and relative density of the synthesized $Mg_{0.8}Cd_{0.2}Fe_{2-x}Sm_xO_4$ samples with $x = 0.00-0.10$.

and relative density ($\rho_R = \rho_B/\rho_T$) of the samples with various Sm concentrations, with the numerical value being listed in Table 2. It shows that density first increases and then decreases, which is in good correspondence with SEM images, validating the tendency for change in the microstructure. It also observed that ρ_R is higher than 90% for all samples, meaning that the synthesized samples are processed with comparatively dense microstructure.

Magnetic properties of processed samples are depicted in Fig. 5. The magnetic hysteresis loops in Fig. 5 (a) reveal that the processed spinel Mg ferrites possess excellent soft magnetic properties, including high saturation magnetization (M_s) and high coercivity (H_c) tuned by the Sm^{3+} ions. As shown in Fig. 5 (b), M_s first displays an upward trend from 20 emu/g to 28.63 emu/g when x increases from 0.00 to 0.06, and then falls back to 24.45 emu/g as x reaches 0.10, whereas H_c displays a negative correlation with M_s when x changes.

It is evident that magnetization is relatively dependent on the amount of Sm^{3+} ions, and magnetization is generally enhanced after comparing the samples with and without Sm^{3+} ions. The increased M_s is related to the morphology. Higher M_s is achieved with larger grain size and less pores [23]. For decreased M_s , as discussed earlier, the inclusion of Sm^{3+} ions leads to further distortions and thus changes the bond angle of Mg-Fe (Sm)-O. Additionally, more pores between grains and lower densification result in reduced saturation magnetization. The obstruction of dissociated magnetic domain wall movement between grains is degraded, causing lowered M_s .

In magnetic materials, three factors determine H_c : shape anisotropy, magnetocrystalline anisotropy, and magnetoelastic anisotropy. Here, the magnetocrystalline anisotropy and magnetoelastic anisotropy mainly account for the change in H_c that first decreases and then increases. The shape anisotropy caused by grains in a unidirectional arrangement has only a small influence on H_c [24]. Generally, the relation between M_s and H_c follows the following Stoner-Wohlfarth theory, which is based on experimental results [5,25].

$$H_c = 0.98K/M_s$$

Where K is the anisotropy constant.

Fig. 6 shows the frequency dependence of complex permeability and permittivity of the processed ferrites on various values of x . Fig. 6 (a) depicts the frequency dependence of magnetic spectra of the samples substituted with various concentrations of Sm^{3+} ions. The real part of the permeability (μ') increases monotonically from approximately 40H/m to 65H/m when x increases from 0.00 to 0.06. After this, μ' decreases to approximately 25H/m when x increases to 0.10. This shows the same change trend as that of M_s . According to the following relationship, the initial permeability, μ , is directly proportional to M_s [26]:

$$\mu \propto \frac{Ms^2}{Ku1 + \lambda s \sigma}$$

Where $Ku1$ is the first-order anisotropy constant. λs and σ represent the magnetostriction coefficient and internal stress, respectively. $\lambda s \sigma$ is always small enough to be neglected. Thus, permeability mainly depends on M_s . In addition, it can be observed that the peak frequency point, i.e. the resonance frequency, F_r of μ' increases as μ' decreases. This is due to the Snoek's limit [27]:

$$F_r \propto \frac{1}{\mu}$$

It is another factor that the value of permeability associated with

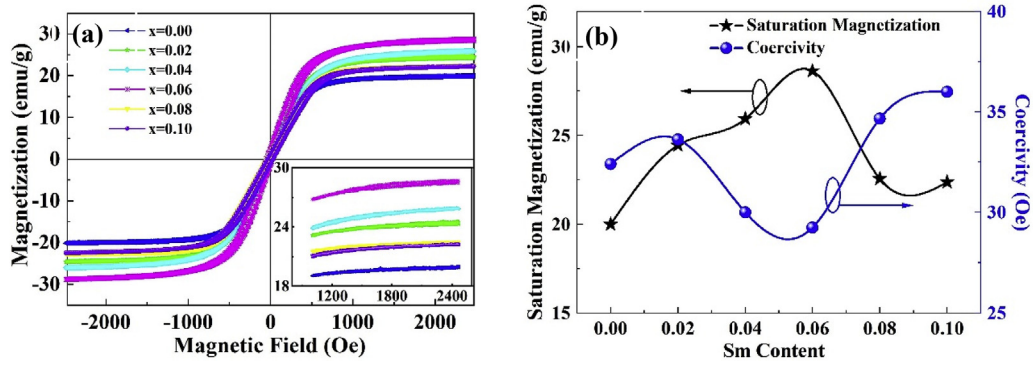


Fig. 5. Magnetic properties of the synthesized $Mg_{0.8}Cd_{0.2}Fe_{2-x}Sm_xO_4$ samples with various Sm contents ($x = 0.00-0.10$). (a) Magnetic hysteresis loops, (b) saturation magnetization and coercivity.

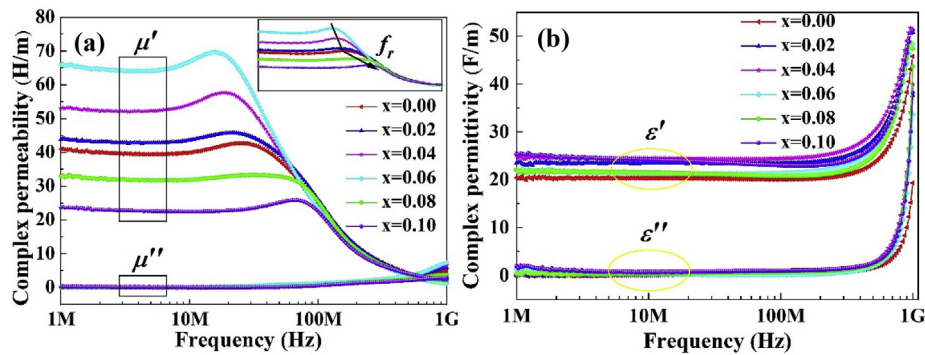


Fig. 6. Magnetic and dielectric spectra for the synthesized $Mg_{0.8}Cd_{0.2}Fe_{2-x}Sm_xO_4$ samples with $x = 0.00-0.10$. (a) Complex magnetic permeability, (b) complex dielectric permittivity.

permittivity should not be too large.

The imaginary part of permeability (μ'') with an order of magnitude 1×10^{-1} , as shown in Fig. 6 (a), indicates that low temperature sintered samples possess low magnetic loss tangent ($\tan\delta_\mu$), which is derived using the following equation [8]:

$$\tan\delta_\mu = \frac{\mu''}{\mu'}$$

Here, we specifically discuss the low loss of the sample with $x = 0.10$. According to the equation, the value of $\tan\delta_\mu$ of the chosen sample can be calculated to be as low as approximately 3.8×10^{-2} over a long frequency band of 1–100 MHz. This characteristic is attributed to three factors: the eddy current loss tangent $\tan\delta_e$, hysteresis loss tangent $\tan\delta_a$, and the remaining loss tangent $\tan\delta_c$, which make up $\tan\delta_\mu$, as described in the following equation [5]:

$$\tan\delta_\mu = \tan\delta_e + \tan\delta_a + \tan\delta_c$$

Among these factors, $\tan\delta_e$ internally comes from electromagnetic induction generating cover fever and power dissipation, and is closely related to H_c . Adjustment of the microstructure, such as raising the densification or crystal size, can lower $\tan\delta_e$. The reduction in the area of hysteresis loop and H_c mainly contributes to the lowering of $\tan\delta_a$. $\tan\delta_c$ is comparatively easy to tune using physical methods such as careful shaping, and ensuring grinding thickness uniformity. Overall, in this study low $\tan\delta_\mu$ is obtained through densification sintering.

The dielectric spectra in Fig. 6 (b) show a flat response over a long frequency band of 1–500 MHz. The value of the real part of the permittivity (ϵ') floats in the small range of 20–25 F/m with three

distinct regions. Specifically, it first increases from approximately 20 F/m to 25 F/m when x increases to 0.04, and then decreases to approximately 21.5 F/m when x increases up to 0.08. Finally, ϵ' again becomes approximately 25 F/m when x is 0.10. During the first stage, the increase in ϵ' is attributed to the increase in grain size and denser grain arrangement. During the second stage, the grain growth is suppressed by the introduction of Sm, resulting in the formation of small-size grains. Consequently, ϵ' decreases [28]. During the last stage, the increase in ϵ' is mainly due to the interfacial polarization and intrinsic electric dipole polarization [29].

The imaginary part of permittivity (ϵ'') shows excellent stable and low values covering 1 MHz–500 MHz. Low $\tan\delta_\epsilon$ is also achieved for all the samples, especially the value of the $x = 0.10$ sample reaches 4×10^{-3} , which is a very low order of magnitude for ferrite materials. Like $\tan\delta_\mu$, $\tan\delta_\epsilon$ is calculated using the following relationship [16]:

$$\tan\delta_\epsilon = \frac{\epsilon''}{\epsilon'}$$

Microstructure always plays a key role in determining the dielectric loss [30], for example, uniform grain boundaries between crystals and polycrystalline material can reduce ϵ'' [31], lower porosity will also lead to lower ϵ'' . The equation summarized as follows illustrates their relationship [30]:

$$\tan\delta_\epsilon = (1 - P)\tan\delta_0 + CP^n$$

Where P is the porosity, $\tan\delta_0$ is the dielectric loss tangent of the material with full densification, and C is a material dependent constant. A reasonable explanation is given by equation, based on

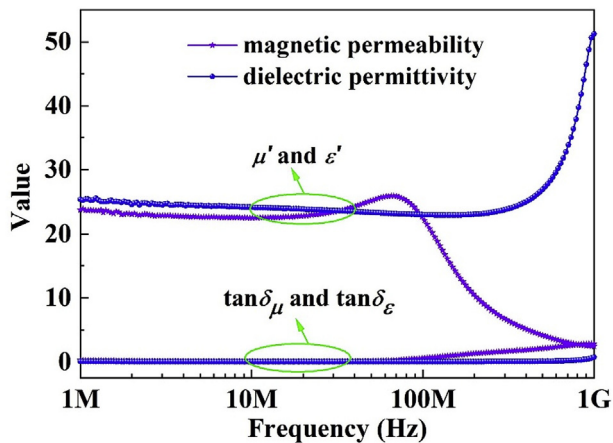


Fig. 7. Equivalent permeability and permittivity and low loss properties of the $\text{Mg}_{0.8}\text{Cd}_{0.2}\text{Fe}_{2-x}\text{Sm}_x\text{O}_4$ samples with $x = 0.10$.

both intrinsic and extrinsic aspects, of which $(1-P)\tan\delta_0$ is the intrinsic loss depending on the formation of the material, and external loss CP^n is small enough to be neglected with large n and small P ($0 \leq P \leq 1$). Thus, densification sintering also give rise to low dielectric loss.

Equivalent permeability and permittivity and low-loss properties of the sample for $x = 0.10$ are shown in Fig. 7, which is extracted from Fig. 6. We see that both μ' and ϵ' ($\mu' \approx 23\text{H/m}$, $\epsilon' \approx 25\text{F/m}$) are nearly equal over a wide frequency band of 1 MHz–100 MHz. Therefore, great impedance matching between antenna and free space is achieved as discussed in the introduction. At the same time, low loss ($\tan\delta_\epsilon \approx 0.004$, $\tan\delta_\mu \approx 0.038$) over long frequency range exhibited by the sample ensures good insulativity and electro-magnetic performance, resulting in less energy loss generation from heat.

4. Conclusion

The formula for Sm substituted Mg–Cd spinel ferrites ($\text{Mg}_{0.8}\text{Cd}_{0.2}\text{Fe}_{2-x}\text{Sm}_x\text{O}_4$) with 2.5 wt% Bi_2O_3 dopant was proposed to realize equivalent ϵ' and μ' , and low loss properties. Experimentally, ϵ' and μ' were tailored to be nearly equal ($\mu' \approx 23\text{H/m}$, $\epsilon' \approx 25\text{F/m}$) covering the frequency range from 1 MHz to 100 MHz. Low $\tan\delta_\mu$ and $\tan\delta_\epsilon$ ($\tan\delta_\epsilon \approx 0.004$, $\tan\delta_\mu \approx 0.038$) were also obtained over the same long frequency range. In addition, excellent magnetization, including enhanced M_s (24.45 emu/g) and appropriate H_c (36 Oe), should ensure excellent magneto-dielectric performance of the material in applications. These characteristics validate that ferrites processed at low temperature possess dielectric and magnetic properties suited to a broad range of applications involving HF and VHF radiofrequency communications.

Author contributions section

This work is finished in collaboration with all the authors listed in the article, and the following is the detailed contributions of each author.

Gongwen Gan: proposing the idea, designing experiment, writing article.

Dainan Zhang: conducting experiment and writing.

Jie Li: responsible for most measurements.

Gang Wang: plotting.

Xin Huang: doing partial experiment.

Yan Yang: doing partial experiment.

Yiheng Rao: doing partial measurement.

Fang Xu: providing some technical guidance for experiment and helping to do some experiments.

Xueying Wang: data processing.

Huaiwu Zhang: revising the article.

Ray T. Chen: revising, checking and finalizing the article.

Declaration of competing interest

The authors declare that they have no known competing financial interests or personal relationships that could have appeared to influence the work reported in this paper.

Acknowledge

This work was supported by National Key Scientific Instrument and Equipment Development Project No.51827802, and by Major Science and Technology projects in Sichuan Province No. 2019ZDX0026, and by the National Natural Science Foundation of China No. 51872041, and by Foundation for University Teacher of Education of China No. ZYGX2019J011.

References

- [1] L.B. Kong, Z.W. Li, G.Q. Lin, Y.B. Gan, Electrical and magnetic properties of magnesium ferrite ceramics doped with Bi_2O_3 , *Acta Mater.* (2007), <https://doi.org/10.1016/j.actamat.2007.08.011>.
- [2] A. Saini, K. Rana, A. Thakur, P. Thakur, J.L. Mattei, P. Queffelec, Low loss composite nano ferrite with matching permittivity and permeability in UHF band, *Mater. Res. Bull.* 76 (2016) 94–99, <https://doi.org/10.1016/j.materresbull.2015.12.002>.
- [3] N.H.M. Yunus, J. Yunus, A. Pawi, Z.A. Rhazali, J. Sampe, Investigation of micromachined antenna substrates operating at 5 GHz for RF energy harvesting applications, *Micromachines* 10 (2019), <https://doi.org/10.3390/mi10020146>.
- [4] S. Sahandabadi, S.V.A.D. Makki, Mutual coupling reduction using complementary of SRR with wire MNG structure, *Microw. Opt. Technol. Lett.* 61 (2019) 1231–1234, <https://doi.org/10.1002/mop.31717>.
- [5] Y. Peng, X. Wu, Z. Chen, W. Liu, F. Wang, X. Wang, Z. Feng, Y. Chen, V.G. Harris, BiFeO_3 tailored low loss M-type hexaferrite composites having equivalent permeability and permittivity for very high frequency applications, *J. Alloy. Comp.* (2015), <https://doi.org/10.1016/j.jallcom.2015.01.026>.
- [6] G. Gan, D. Zhang, Q. Zhang, G. Wang, X. Huang, Y. Yang, Y. Rao, J. Li, F. Xu, X. Wang, R.T. Chen, H. Zhang, Influence of microstructure on magnetic and dielectric performance of Bi_2O_3 -doped $\text{Mg}[\text{sbn}]_2\text{Cd}$ ferrites for high frequency antennas, *Ceram. Int.* (2019), <https://doi.org/10.1016/j.ceramint.2019.03.098>.
- [7] Y. Lin, X. Liu, H. Yang, F. Wang, C. Liu, X. Wang, Laminated $\text{SrTiO}_3\text{-Ni}_0.8\text{Zn}_0.2\text{Fe}_2\text{O}_4$ magneto-dielectric composites for high frequency applications, *J. Alloy. Comp.* (2016), <https://doi.org/10.1016/j.jallcom.2016.07.225>.
- [8] G. Gan, H. Zhang, Q. Li, J. Li, X. Huang, F. Xie, F. Xu, Q. Zhang, M. Li, T. Liang, G. Wang, Low loss, enhanced magneto-dielectric properties of Bi_2O_3 doped Mg–Cd ferrites for high frequency antennas, *J. Alloy. Comp.* (2018), <https://doi.org/10.1016/j.jallcom.2017.12.002>.
- [9] P. Godara, A. Agarwal, N. Ahlawat, S. Sanghi, Crystal structure refinement, dielectric and magnetic properties of Sm modified BiFeO_3 multiferroic, *J. Mol. Struct.* (2015), <https://doi.org/10.1016/j.molstruc.2015.05.022>.
- [10] V. Jagadeesha Angadi, B. Rudraswamy, K. Sadhana, K. Praveena, Effect of $\text{Sm}^{3+}\text{-Gd}^{3+}$ co-doping on dielectric properties of Mn–Zn ferrites synthesized via combustion route, *Mater. Today Proc.* (2016), <https://doi.org/10.1016/j.matpr.2016.04.124>.
- [11] P. Sharma, A. Verma, R.K. Sidhu, O.P. Pandey, Influence of Nd^{3+} and Sm^{3+} substitution on the magnetic properties of strontium ferrite sintered magnets, *J. Alloy. Comp.* (2003), [https://doi.org/10.1016/S0925-8388\(03\)00390-6](https://doi.org/10.1016/S0925-8388(03)00390-6).
- [12] M.A. Khan, M.U. Islam, M. Ishaque, I.Z. Rahman, Effect of Tb substitution on structural, magnetic and electrical properties of magnesium ferrites, *Ceram. Int.* 37 (2011) 2519–2526, <https://doi.org/10.1016/j.ceramint.2011.03.063>.
- [13] T. Krishnaveni, S.R. Murthy, F. Gao, Q. Lu, S. Komarneni, Microwave hydrothermal synthesis of nanosize Ta_2O_5 added Mg–Cu–Zn ferrites, *J. Mater. Sci.* 41 (2006) 1471–1474, <https://doi.org/10.1007/s10853-006-7488-5>.
- [14] G. Wang, H. Zhang, C. Liu, H. Su, J. Li, X. Huang, G. Gan, F. Xu, Low temperature sintering and microwave dielectric properties of novel temperature stable $\text{Li}_3\text{Mg}_2\text{NbO}_6\text{-}0.1\text{TiO}_2$ ceramics, *Mater. Lett.* 217 (2018), <https://doi.org/10.1016/j.matlet.2018.01.049>.
- [15] M.K. Kokare, N.A. Jadhav, V. Singh, S.M. Rathod, Effect of Sm^{3+} substitution on the structural and magnetic properties of Ni–Co nanoferrites, *Opt. Laser Technol.* (2019), <https://doi.org/10.1016/j.optlastec.2018.10.045>.

- [16] E. Ateia, M.A. Ahmed, A.K. El-Aziz, Effect of rare earth radius and concentration on the structural and transport properties of doped Mn-Zn ferrite, *J. Magn. Magn. Mater.* (2007), <https://doi.org/10.1016/j.jmmm.2006.08.014>.
- [17] M.A. Dar, D. Varshney, Effect of d-block element Co²⁺ substitution on structural, Mössbauer and dielectric properties of spinel copper ferrites, *J. Magn. Magn. Mater.* 436 (2017) 101–112, <https://doi.org/10.1016/j.jmmm.2017.04.046>.
- [18] M. Qian, Sintering and related phenomena, *J. Occup. Med.* (2017), <https://doi.org/10.1007/s11837-017-2293-y>.
- [19] B. Deka, S. Ravi, D. Pamu, Evolution of structural transition, grain growth inhibition and collinear antiferromagnetism in (Bi_{1-x}Sm_x)FeO₃ (x = 0 to 0.3) and their effects on dielectric and magnetic properties, *Ceram. Int.* (2017), <https://doi.org/10.1016/j.ceramint.2017.09.046>.
- [20] A.B. Gadkari, T.J. Shinde, P.N. Vasambekar, Synthesis, characterization and magnetic properties of La³⁺ added Mg-Cd ferrites prepared by oxalate coprecipitation method, *J. Alloy. Comp.* (2011), <https://doi.org/10.1016/j.jallcom.2010.08.155>.
- [21] M.F. Valan, A. Manikandan, S.A. Antony, Microwave combustion synthesis and characterization studies of magnetic Zn_{1-x}Cd_xFe₂O₄ (0 ≤ x ≤ 0.5) nanoparticles, *J. Nanosci. Nanotechnol.* (2014), <https://doi.org/10.1166/jnn.2015.9801>.
- [22] N. Yasmin, M. Mirza, S. Muhammad, M. Zahid, M. Ahmad, M.S. Awan, A. Muhammad, Influence of samarium substitution on the structural and magnetic properties of M-type hexagonal ferrites, *J. Magn. Magn. Mater.* (2018), <https://doi.org/10.1016/j.jmmm.2017.09.005>.
- [23] K. Chakrabarti, K. Das, B. Sarkar, S. Ghosh, S.K. De, G. Sinha, J. Lahtinen, Enhanced magnetic and dielectric properties of Eu and Co co-doped BiFeO₃ nanoparticles, *Appl. Phys. Lett.* (2012), <https://doi.org/10.1063/1.4738992>.
- [24] S.E. Shirsath, S.S. Jadhav, B.G. Toksha, S.M. Patange, K.M. Jadhav, Influence of Ce⁴⁺ ions on the structural and magnetic properties of NiFe₂O₄, *J. Appl. Phys.* 110 (2011), <https://doi.org/10.1063/1.3603004>.
- [25] L.J. Giacomello, Physics of magnetism, *Proc. IEEE* (2008), <https://doi.org/10.1109/proc.1965.4557>.
- [26] J. Lee, J. Heo, J. Lee, Y. Han, Design of small antennas for mobile handsets using magneto-dielectric material, *IEEE Trans. Antennas Propag.* 60 (2012) 2080–2084, <https://doi.org/10.1109/TAP.2012.2186271>.
- [27] Y. Bai, J. Zhou, Z. Gui, L. Li, L. Qiao, The physic properties of Bi-Zn codoped Y-type hexagonal ferrite, *J. Alloy. Comp.* 450 (2008) 412–416, <https://doi.org/10.1016/j.jallcom.2006.10.122>.
- [28] J. Xu, G. Ji, H. Zou, Y. Song, S. Gan, Influence of Sm-substitution on structure and electromagnetic properties of Ba_{3-x}Sm_xCo₂Fe₂₄O₄₁ powders, *J. Magn. Magn. Mater.* (2011), <https://doi.org/10.1016/j.jmmm.2010.08.055>.
- [29] J.D. Breeze, J.M. Perkins, D.W. McComb, N.M.N. Alford, Do grain boundaries affect microwave dielectric loss in oxides? *J. Am. Ceram. Soc.* (2009) <https://doi.org/10.1111/j.1551-2916.2009.02932.x>.
- [30] H. Jia, W. Liu, Z. Zhang, F. Chen, Y. Li, J. Liu, Y. Nie, Monodomain MgCuZn ferrite with equivalent permeability and permittivity for broad frequency band applications, *Ceram. Int.* (2017), <https://doi.org/10.1016/j.ceramint.2017.01.129>.
- [31] S.J. Penn, N.M. Alford, A. Templeton, X. Wang, M. Xu, M. Reece, K. Schrapel, Effect of porosity and grain size on the microwave dielectric properties of sintered alumina, *J. Am. Ceram. Soc.* (2005), <https://doi.org/10.1111/j.1151-2916.1997.tb03066.x>.